

Secondary electron emission and self-consistent charge transport and storage in bulk insulators: Application to alumina

X. Meyza and D. Goeuriot

Centre Sciences des Matériaux et des Structures, Ecole Nationale Supérieure des Mines, 158 cours Fauriel, 42023 Saint-Etienne cedex 2, France

C. Guerret-Piécourt^{a)}

Laboratoire de Physico-Chimie des Polymères, UMR-CNRS 5067, Université de Pau, BP 1157, 64013 Pau cedex, France

D. Tréheux

Laboratoire d'Ingénierie et Fonctionnalisation des Surfaces, UMR-CNRS 5621, Ecole Centrale de Lyon, 36 avenue Guy de Collongue, 69134 Ecully cedex, France

H.-J. Fitting

Physics Department, University of Rostock, Universitätsplatz 3, D-18051 Rostock, Germany

(Received 12 May 2003; accepted 4 August 2003)

The self-consistent charge transport in bulk alumina samples during electron beam irradiation is described by means of an iterative computer simulation. Ballistic electron and hole transport as well as their recombination and trapping are included. As a main result the time-dependent secondary electron emission rate $\sigma(t)$ and the spatial distributions of currents $j(x,t)$, charges $\rho(x,t)$, the field $F(x,t)$, and the potential slope $V(x,t)$ are obtained. For bulk insulating samples, the time-dependent distributions approach the final stationary state with $j(x,t) = \text{const} = 0$ and $\sigma = 1$. Especially for low electron beam energies $E_0 = 1$ keV, the incorporation of charges can be controlled by the potential V_G of a vacuum electrode in front of the target surface. Finally, for high electron beam energies, the real negative surface potential $V_0 < 0$ is measured by x-ray bremsstrahlung spectra and the shift of the short wavelength edge. For the initial beam energy $E_0 = 30$ keV, the experimental value $V_0 = -16$ kV is still in good agreement with our simulations. © 2003 American Institute of Physics. [DOI: 10.1063/1.1613807]

I. INTRODUCTION

During the last years, the influence of dielectric polarization on the essential features of dielectric and insulating materials has been investigated more intensively leading, finally, to better understanding and applications of these materials (see, e.g., the conference series on electric charges in nonconductive materials in Ref. 1, and also Ref. 2). One of the subjects of interest is the prediction of electrical charging of insulators under ionizing irradiation as it is of great importance in many fields of modern technology. For instances, the knowledge of such phenomena would help in preventing insulator breakdown mainly responsible for the damage of electronic devices.^{3,4} In electron microscopy, like scanning electron microscopy (SEM) or Auger electron spectroscopy (AES), electron energy loss spectroscopy (EELS), etc., the prediction of the influence of charging is essential to interpret the results of analysis.⁵⁻⁷ The charging of insulators has also to be known in order to manage applications such as electron lithography, electron multipliers, electrets, etc. On the other hand, problems have arisen with the deflection of interstellar dust grains in the magnetic field near the heliopause depending on their surface electric charge.⁸ A

great number of experimental and theoretical investigations have been published on the charging of insulators due to electron bombardment and the related secondary electron emission (SEE). Only for short pulse irradiation, target charging is prevented and the real charging-free secondary electron emission yield $\sigma(E_0)$ as a function of the primary electron energy E_0 can be measured and determined theoretically for various insulators.⁹⁻¹³ However, the charging behavior under permanent electron irradiation is not yet fully understood and the stationary final state is still very complex to describe. Indeed, the total yield approach ($\sigma \geq 1$) is often used to predict the sign (\pm) of charging in the case of stationary electron irradiation, but experimental results are not fully consistent with these predictions.^{14,15} It is of importance to precise the types of theory that have been led to enlighten this phenomenon. One of the first attempts was the planar (one-dimensional) self-consistent charging simulation of our co-author (H.J.F.) already in 1979,¹⁶ later on improved in Ref. 17. These authors use field-dependent attenuation lengths $\lambda(F)$ for the ballistic transport of electrons and holes, which had been found experimentally by means of electron beam induced currents (EBIC) measurements.

Comprehensive Monte Carlo calculations of the self-consistent charging were made by Vicario *et al.*,¹⁸ Ganachaud *et al.*,¹⁹ and Renoud *et al.*²⁰ Of course, these calculations are complex because they deal with the full

^{a)} Author to whom correspondence should be addressed; electronic mail: Christelle.Guerret@univ-pau.fr

simulation of primary electron straggling as well as with the generation and transport of secondary electrons and holes in the self-consistent field. Contrary to the one-dimensional charging model based on Monte Carlo-calculated and experimentally well-prooved attenuation lengths $\lambda(F)$ of electrons and holes, the full Monte Carlo simulation bears more uncertainty in all the theoretical parameters used and, of course, it takes much more time for one simulation run. However, the decisive advantage of the full Monte Carlo simulation is the three-dimensional description of the charging process with the lateral charge spreading in the case of point-like electron beam injection by a very small beam focus. Thus, the above-mentioned authors^{18,20} could demonstrate the buildup by a computer animation.

An approach for more rough estimation is based on the dynamic double layer model (DDLDM) in which the phenomenon is brought to the simplified case of two layers of opposite charge. Complete solutions of the respective equations were achieved by Melchinger *et al.*¹⁴ More recently, Cazaux¹⁵ developed an effective approach of the SEE evolution in insulating samples using this DDLDM.

The present article is aimed to the extension of the planar one-dimensional self-consistent model for thin layers as given in Refs. 16 and 17, now to bulk insulators. It will approach full validity if the electron beam diameter is much larger than the maximum electron penetration depth $R(E_0)$. Unambiguously, this is fulfilled in scanning electron microscopes with a slightly defocused beam. Thus, the one-dimensional simulation can be applied to three-dimensional description of the sample potential in a SEM chamber.²¹ The results will be presented, in particular, for alumina but could be easily adapted to any insulator using the relevant material data available in the literature.

II. THEORETICAL BACKGROUND

The strong charging of insulators under electron beam irradiation is well known, at least, since Malter (1936) discovered the anomalous high secondary electron emission and long-lasting electron postemission from MgO layers.²² A strong positive charging due to the emission of secondary electrons (SEs) from the near-surface regions is responsible for that self-consistent field-enhanced SEE. On the other hand, the deeper injection of primary electrons (PEs) will produce an electron surplus within the bulk of an insulator. The respective charge $\rho(x)$ and field $\mathbf{F}(x)$ distributions maintain the self-consistent charge transport and the SEE emission.

A. Generation of currents and charges

Thus, we should first refer to the injection of primary electrons and their creation of secondary electrons and holes (H). This process for Al_2O_3 is similar to that of SiO_2 as we have described already in Refs. 16 and 17 based on empirical results of the electron penetration process into solids having been obtained by the ‘‘film-bulk method.’’²³ By means of this method the resulting PE current in dependence of the target depth x and the PE initial energie E_0 was found:

$$j_{\text{PE}}(x, E_0) = j_0(1 - \eta) \exp \left[-4.605 \left(\frac{x}{R(E_0, z)} \right)^{p(z)} \right], \quad (1)$$

with j_0 as impinging PE current density and the material parameters for SiO_2 : $\eta \approx 0.2$ the backscattering coefficient, $p \approx 2$ the exponential transmission parameter, and the empirical equation for the maximum electron range R reached by 1% of PE:

$$R/\text{nm} = \frac{900}{\rho^{0.8}} (E_0/\text{keV})^{1.3} \quad \text{for } E_0 < 8 \text{ keV}, \quad (2a)$$

$$R/\text{nm} = \frac{450}{\rho^{0.9}} (E_0/\text{keV})^{1.7} \quad \text{for } E_0 \geq 8 \text{ keV}. \quad (2b)$$

R is given in nm, the target mass density ρ in g/cm^3 , and the electron beam energy E_0 in keV. In Ref. 23 one can find the respective quantities of any material when knowing the mass density and the PE backscattering ratio $\eta(E_0)$.

The generation rate $g_i(x, E_0)$ of inner secondary electrons is proportional to the spatial energy loss dE/dx of the impinging and straggling primary electrons, i.e., proportional to the spatial PE energy transfer to the target volume:

$$g_i(x, E_0) = \alpha \frac{1}{E_i} \frac{dE}{dx}, \quad (3)$$

where E_i is the mean creation energy for one SE and α a yield factor of nearly a unit. According to Klein²⁴ and Alig and Bloom²⁵ the SE creation energy increases with the energy gap E_g of a given target material

$$E_i \approx 3E_g + 1 \text{ eV}, \quad (4)$$

resulting in $E_i \approx 28$ eV for Al_2O_3 with $E_g = 9$ eV. Then, with Eq. (3) and empirical expressions for dE/dx from Ref. 23, we may write the SE creation rate in Al_2O_3 in the form of a semiempirical equation

$$g_i/\text{\AA} = 0.146(E_0/\text{keV})^{-0.3} \exp \left[-7.5 \left(\frac{x}{R} - 0.3 \right)^2 \right]. \quad (5)$$

This is a Gaussian distribution with the maximum shifted by $0.3R$ from the surface into the target volume. Assuming an isotropic SE generation, one half of the created SE: $1/2 j_0 g_i(x, E_0) \Delta x$ will move into the bulk sample, i.e., in the direction towards the sample support and the other half towards the sample surface. Then, the respective continuity equation in one-dimensional form for any SE or hole currents in the transmission (T) direction towards the sample substrate (holder) or in reverse (R) direction towards the surface looks very simple:

$$j_T^R(x) = [j_T^R(x \pm \Delta x) + \frac{1}{2} j_0 g_i(x) \Delta x] W(x), \quad (6)$$

with the first term in the brackets for the convection part and the second one for the generation of inner SEs or holes followed by the overall attenuation probability $W(x)$ of the charge carriers over the small distance Δx in the target depth x . This attenuation probability will be described separately below.

Thus, the current possesses sources with $g_i(x)$ as well as drains due to the attenuation $W(x)$. Introducing the exces-

sive charge $\Delta\rho$ into the continuity equation we get for the actual charge change over the time Δt in the depth Δx and for the time t :

$$\Delta\rho(x,t) = -\frac{j(x+\Delta x,t) - j(x-\Delta x,t)}{2\Delta x} \Delta t. \quad (7a)$$

Adding this excessive charge $\Delta\rho$ to the already present charge:

$$\rho(x,t) = \rho(x,t-\Delta t) + \Delta\rho(x,t), \quad (7b)$$

we may obtain the electrical field distribution $F(x)$ via the Poisson equation, i.e., by integration of the charges:

$$F(x,t) = \frac{1}{\varepsilon_0\varepsilon_r} \int_0^x \rho(x',t) dx'. \quad (8)$$

Further on, the related potential slope $V(x,t)$ is given by

$$V(x,t) = \int_d^x F(x',t) dx'. \quad (9)$$

Because the sample support should be grounded, $V(x=d) = 0$, the integration starts at the sample support electrode in the depth d denoting the sample surface with $x=0$ and the back electrode with the target thickness $x=d$.

B. Attenuation of currents

In context with Eq. (6) we have introduced the overall attenuation probability W . First of all, W will depend on the actual field strength F enhancing or diminishing the mean attenuation length $\lambda(F)$. This very important transport parameter has been investigated experimentally^{26,27} as well as calculated by Monte Carlo simulations.^{28–30}

Thus, the field-dependent attenuation probability indicated for electrons by (E) in transmission (T) and reverse (R) direction is

$${}^R W_{EF} = \exp\left[-\frac{\Delta x}{\lambda_E(\pm F)}\right] = \exp\left[-\frac{\Delta x}{\lambda_{E,0} \exp(\pm \beta_E F)}\right]. \quad (10a)$$

For holes (H) we can write the respective relation:

$${}^R W_{HF} = \exp\left[-\frac{\Delta x}{\lambda_H(\mp F)}\right] = \exp\left[-\frac{\Delta x}{\lambda_{H,0} \exp(\mp \beta_H F)}\right], \quad (10b)$$

including the mean-field-dependent attenuation length λ_E for electrons and λ_H for holes with their field-free values $\lambda_{E,0}$ and $\lambda_{H,0}$ as well as the field-enhancing factors β_E and β_H , respectively.

Whereas the mean attenuation length for electrons $\lambda_E(\pm F)$ is enhanced for positive fields $F > 0$ in reverse (R) motion towards the surface, it is diminished for transmission (T) direction towards the sample support. Negative fields $F < 0$ will result in opposite relations for electrons, i.e., enhancement in (T) and retarding in the (R) direction, respectively. Of course, for holes (H) the relations for ${}^R W_{HF}$ in Eq. (10b) should be given vice versa, i.e., with an opposite sign with respect to electrons in Eq. (10a).

Further on, we should consider electron-hole recombination as a second kind of current attenuation. With the related

recombination cross sections $S_{EH} = S_{HE}$, we can write the recombination probability for electrons over the distance Δx :

$$W_{EH} = \exp\left[-\frac{\rho_H}{e_0} S_{EH} \Delta x\right], \quad (11a)$$

as well as for holes:

$$W_{HE} = \exp\left[-\frac{\rho_E}{e_0} S_{HE} \Delta x\right]. \quad (11b)$$

Now the charges are required separately for electrons ρ_E and for holes ρ_H , respectively. Another attenuation of the currents is given by the trapping probability to localized electron states (traps) with an overall concentration $N_{E,0}$ and an actual occupation N_E :

$$W_{EE} = \exp\{-[N_{E,0} - N_E(x)] S_{EE} \Delta x\}. \quad (12a)$$

$N_{H,0}$ and N_H denote for hole concentrations, respectively:

$$W_{HH} = \exp\{-[N_{H,0} - N_H(x)] S_{HH} \Delta x\}. \quad (12b)$$

S_{EE} and S_{HH} hold for the capture cross sections for electrons and holes, respectively.

Finally, we can write the current of Eq. (6) explicitly for electrons (E) in the reverse (R) and transmission (T) direction

$$j_{ET}^{ER}(x) = [j_{ET}^{ER}(x \pm \Delta x) + \frac{1}{2} j_0 g_i(x) \Delta x] {}^R W_{EF} W_{EH} W_{EE}, \quad (13a)$$

as well as for holes (H):

$$J_{HT}^{HR}(x) = [j_{HT}^{HR}(x \pm \Delta x) + \frac{1}{2} j_0 g_i(x) \Delta x] {}^R W_{HF} W_{HE} W_{HH}, \quad (13b)$$

with the respective expressions for the different kinds of attenuation from Eqs. (10)–(12).

The overall current $j(x)$ in the depth x is given by summation of the several components of Eqs. (1), (13a), and (13b):

$$j(x) = -j_{PE}(x) - j_{ET}(x) + j_{ER}(x) + j_{HT}(x) - j_{HR}(x), \quad (14)$$

resulting in the positive sign for positive charges moving in the x direction, i.e., transmission. This current can be inserted into the continuity Eq. (7), providing the excessive charge $\Delta\rho(x)$ as well as via Eq. (8) the respective field distribution $F(x)$, and the potential slope $V(x)$ by means of Eq. (9).

III. SIMULATION OF THE CHARGING PROCESS

The simulation procedure should be oriented to real experimental conditions. In Fig. 1 the scheme of a secondary electron microscope chamber is presented showing the respective currents of primary electrons I_0 , of the total secondary emission σI_0 with $\sigma = \eta + \delta$ as the sum of backscattered electrons (BEs) (η) and true SE (δ) released from the target material. A certain part of emitted electrons can be backscattered or reemitted from the microscope chamber or from a negatively biased electronic grid. These electrons are called tertiary electrons (TEs).

The insulating target, of course, allows three currents to the grounded support: an instationary displacement current of polarization I_P , a real conduction current I_C through the

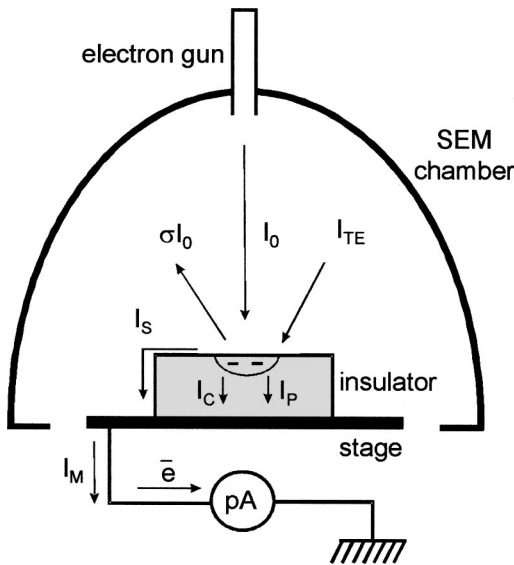


FIG. 1. Electron irradiation of an insulating target in a scanning electron microscope (SEM): I_0 , incident PE current; σI_0 , backscattered (BE) and secondary (SE) part; I_{TE} , tertiary electrons backscattered from the chamber; I_S , surface leakage current; I_C , real conduction current; I_P , instationary displacement current due to charge trapping and incorporation; and I_M , sample stage current.

bulk to the metallic support, as well as a surface leakage current I_S . In their sum they are forming the overall target support current I_M :

$$I_M = I_P + I_C + I_S. \tag{15}$$

The directions of the injected PE current j_{PE} , the inner secondary electron current j_{SE} and the respective hole current j_H are schematically presented in Fig. 2. However, in our case of a bulk Al_2O_3 target, the relatively large thickness of $d = 3$ mm will not allow either a real conduction current j_C to the support or a Fowler–Nordheim (FN) tunneling injection

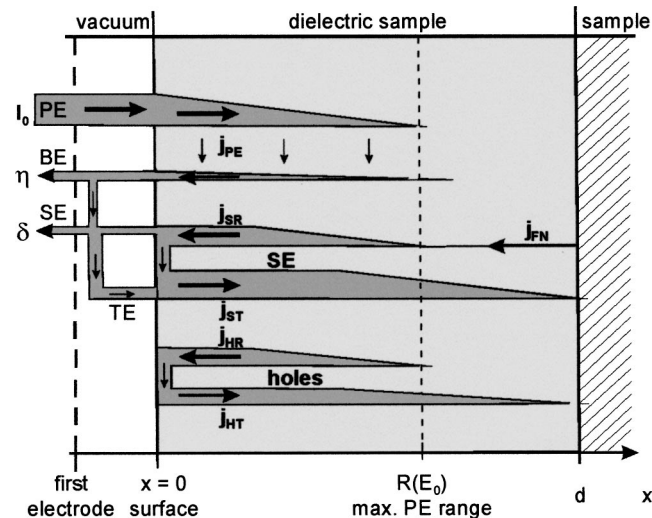


FIG. 2. Scheme of currents in an insulating sample of thickness d during electron irradiation with primary electrons (PEs). The currents of inner secondary electrons (SEs) and holes (H) are given in the forward (T : transmission) and in the reverse (R) direction, see Eq. (13). The total reemission fraction $\sigma = \eta + \delta$ of backscattered electrons (BEs) and SE is diminished by tertiary electrons (TEs).

current j_{FN} from the metallic support into the insulator. The latter one appears only for thin layers $d < 300$ nm and $\sigma > 1$ connected with strong positive charging, see Refs. 16 and 17.

On the other hand, at the surface barrier with an electron affinity χ a certain fraction P_S of incident inner secondary electrons with an energy \bar{E}_{SE} will be reflected:

$$P_S = \sqrt{\chi / \bar{E}_{SE}},$$

the other part,

$$P_{SE} = 1 - \sqrt{\chi / \bar{E}_{SE}},$$

is emitted as secondary electrons over the surface barrier into the vacuum.³¹ For Al_2O_3 with $\chi \approx 0.9$ eV and $\bar{E}_{SE} \approx 6$ eV we get $P_S \approx 0.39$ for the surface reflection coefficient and $P_{SE} = 0.61$ for the SE emission probability.

Furthermore, in the presence of a screening or retarding grid or any vacuum electrode, even, by the SEM chamber itself, biased to a potential V_G less than the actual surface potential $V_0 = V(x=0)$ of the sample surface, i.e., only for $V_G < V_0$, we observe a SE retarding field current reverse to the surface of a rate

$$P_G = 1 - \exp \frac{V_G - V_0}{V_{SE}}, \tag{16}$$

as already introduced in Refs. 16 and 17. With Eq. (16) and $e_0 V_{SE} \approx 5$ eV as the mean kinetic energy of emitted SEs, we may characterize the retarding field curve of SEs.

Thus, we get the boundary conditions of the SE current at the surface $x=0$ with the possibility of twofold reflection at the surface with P_S and at the negative grid with P_G :

$$j_{ET}(x=0) = j_{ER}(x=0) [P_S + (1 - P_S)P_G]. \tag{17}$$

Both of these reflections of reverse (R) moving electrons at the surface and at a retarding electrode are indicated with TEs in Fig. 2. Further on, we should assume that holes are reflected entirely at the surface barrier. So we get:

$$j_{HT}(x=0) = j_{HR}(x=0). \tag{18}$$

When calculating the current balance across the layer according to Eqs. (13a) and (13b), we always have to start with the reverse current j_R at its beginning in the volume behind the maximum excitation depth $R(E_0)$, then going towards the surface and starting the transmission current j_T with the reflection parts of j_R at the surface, see Eq. (17).

After summing up all currents $j(x,t)$ over all x for a certain time t according Eq. (14), we should calculate the respective charges $\rho(x,t)$, fields $F(x,t)$ and potentials $V(x,t)$ as given by Eqs. (7)–(9). Then, we repeat this procedure in an iteration cycle until we get a stationary-like state for the actual irradiation time t . Afterwards, we increase t by Δt and repeat the iteration cycle. The final stationary irradiation state in an insulator is reached when no changes of the overall current along x are observed, i.e., $j(x,t) = \text{const}$, or $\text{div } \mathbf{j} = 0$. Then, also the charge, field, and potential distributions are not changing anymore with time. All is in a stationary equilibrium, in the final steady state.

TABLE I. Material parameters of Al_2O_3 used in the present simulation.

Al_2O_3 material parameters	Unit	Value	Symbol	References
Mass density	(g/cm^3)	3.98	ρ	
Electrical permittivity		10	ϵ_r	32–33
Energy band gap	(eV)	9	E_g	34
Mean ionization energy	(eV)	28	E_i	23–24
Electron affinity	(eV)	0.9	χ	35
SE mean attenuation length	(nm)	5	$\lambda_{E,0}$	16
Hole mean attenuation length	(nm)	2	$\lambda_{H,0}$	16
SE attenuation field factor	(cm/MV)	4.6	β_E	16
Hole attenuation field factor	(cm/MV)	0.8	β_H	16
$e-h$ recombination cross section	(10^{-13} cm^2)	1	$S_{EH}=S_{HE}$	36
Concentration of electron traps	(10^{17} cm^{-3})	1–5	$N_{E,0}$	20, 37–39
Concentration of hole traps		Not considered	$N_{H,0}$	
Trapping cross section of electrons	(10^{-15} cm^2)	1	S_{EE}	20, 37–39
Trapping cross section of holes		Not considered	S_{HH}	

IV. COMPUTATIONAL RESULTS

The simulations of the self-consistent charge transport were performed for 3-mm-thick alumina samples by means of the material parameters given in Table I with their references extended by Refs. 32–39. We look first to the positive charging at a low electron beam energy $E_0=1$ keV, presented in Fig. 3. There we see the time evolution of the current $j(x,t)$ as well as the respective charge $\rho(x,t)$ and field $F(x,t)$ distributions. Obviously, we obtain a suppression of the currents $j(x,t)$ with time t , Fig. 3(a), caused by retarding and reinjection of SE due to a positively charged sample surface with respect to the grounded grid $V_G=0$. This process has been described in context with Eq. (17). The resulting emission current $j(x<0)$ becomes zero and the SE rate approaches $\sigma=1$. Thus, the SEE is blocked and the positive charging becomes stable after about 50 ms, see Fig. 3(b). Due to reinjected secondary electrons the charge distribution shows a minus–plus–minus structure. However, the positive charges are only slightly prevailing the negative ones, leading to a relatively small positive surface potential $V_0 \approx +4.34$ V [as we will see later on in Fig. 6(a)], and an almost zero-field strength towards the sample support, Fig. 3(c). We find a contrary behavior for a high electron beam energy and related negative charging. In Fig. 4, the respective current $j(x,t)$, charge $\rho(x,t)$, and field $F(x,t)$ distributions are presented for an initial beam energy $E_0=30$ keV. Very obviously, with increasing time t the overall current $j(x,t)$ is more and more restricted to near-surface regions. Finally, in the stationary state $j(x,t)=\text{const}=0$ the irradiation depth has decreased from $4.5 \mu\text{m}$ at the beginning $t=0$ to about $0.8 \mu\text{m}$ for $t>100$ ms, Fig. 4(a). Looking to the incorporated charge distribution $\rho(x,t)$ [Fig. 4(b)], we recognize strongly prevailing negative charges correlated with negative field strengths over the bulk volume $x>1 \mu\text{m}$, Fig. 4(c). Due to secondary electron emission into vacuum from a mean escape depth of $\lambda_{E0}=5$ nm beneath the surface of the insulator the charge distribution in this zone indicates an electron deficit, i.e., positive charge storage, as we see in Fig. 5, which has been zoomed to nm scale presentation. Nevertheless, the surface potential $V_0(x \rightarrow 0)$ in this region ap-

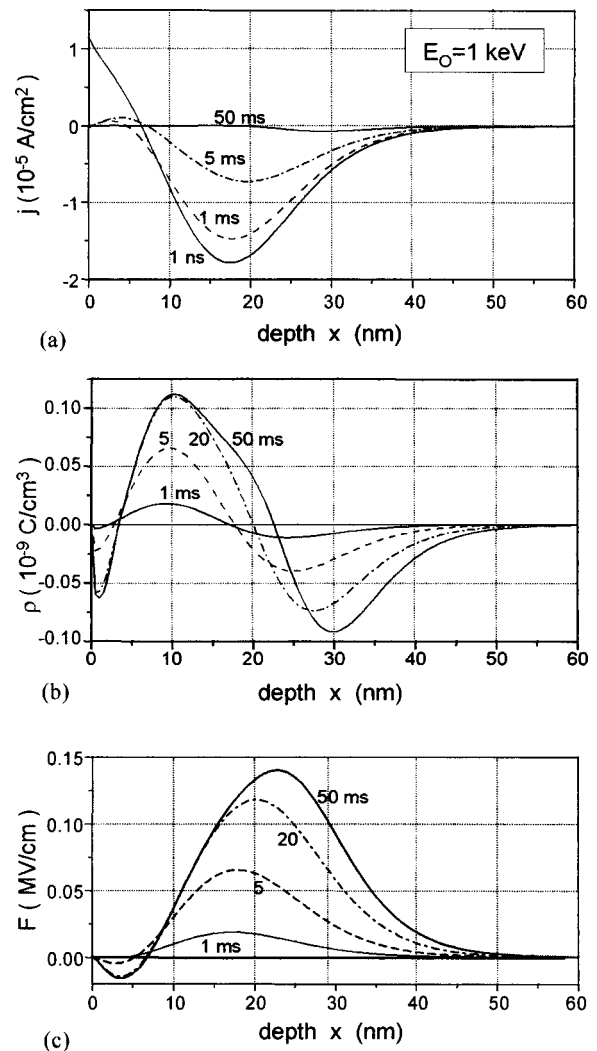


FIG. 3. Low energy $E_0=1$ keV electron irradiation and the related evolution (a) of internal currents j , (b) charge distributions ρ , and (c) field F ; incident current density $j_0=10^{-5} \text{ A}/\text{cm}^2$.

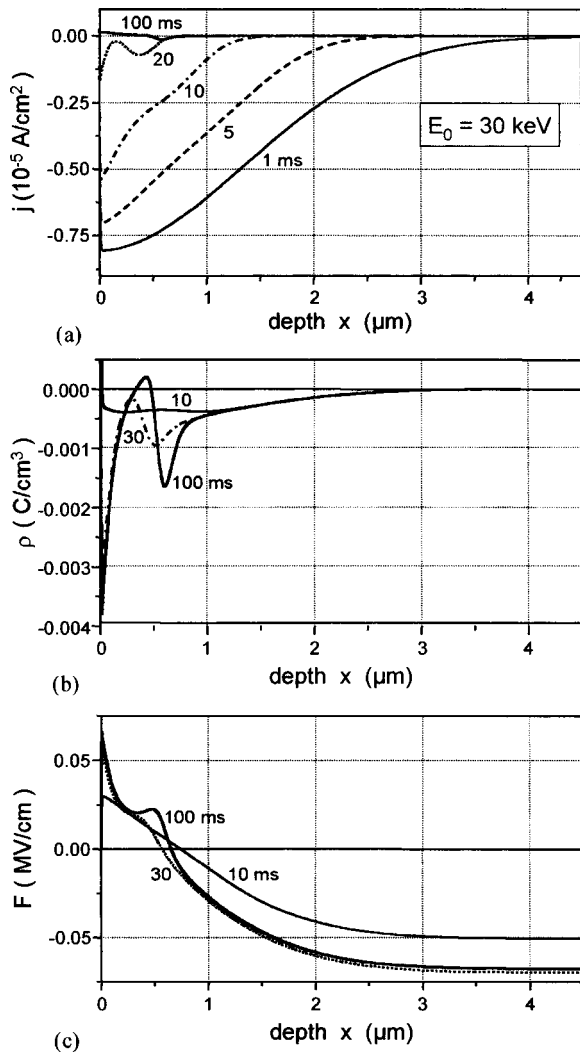


FIG. 4. High energy $E_0 = 30 \text{ keV}$ electron irradiation and the related evolution of (a) internal currents j , (b) charge distributions ρ , and (c) field F ; incident current density $j_0 = 10^{-5} \text{ A/cm}^2$.

proaches high negative values of about $V_0 \approx -22 \text{ kV}$, Fig. 6(b). Of course, this negative surface potential is responsible for the electron beam deceleration from originally $E_0 = 30 \text{ keV}$ down to only $E'_0 \approx 8 \text{ keV}$. Indeed, this diminishes the irradiation depth zone, as we see in Fig. 4(a).

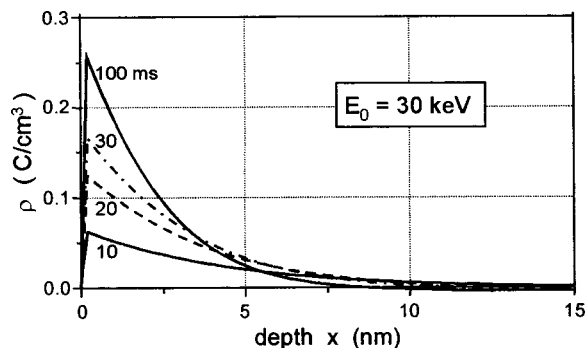


FIG. 5. Positively charged surface region due to forced SE escape in spite of high PE energy $E_0 = 30 \text{ keV}$, but due to an overall negative repulsing charge; zoomed in the nm scale.

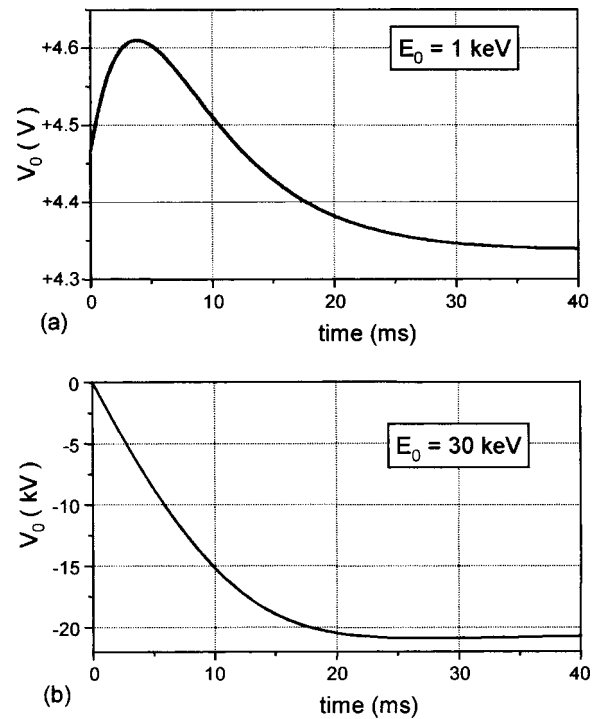


FIG. 6. Surface potential V_0 as a function of the irradiation time t ; with beam energies (a) $E_0 = 1 \text{ keV}$ and (b) 30 keV , and incident current densities $j_0 = 10^{-5} \text{ A/cm}^2$, please note the different voltage scales in V and kV.

Moreover, because of the positive surface charge, there is a small potential decay for electrons towards the surface, maintaining an enhanced SEE and leading finally to the stationary steady state with $\sigma = \eta + \delta = 1$ and the overall current $j(x, t) = 0$ over the entire volume and for all times $t \geq 100 \text{ ms}$.

V. DISCUSSION

From the current $j(x, t)$ and potential $V(x, t)$ distributions of the previous part, we may deduce the respective secondary electron emission rate $\sigma(t)$ as well as the surface potential $V_0(t) = V(x=0, t)$. Both quantities are accessible from outside the sample and can be proved directly by measurements.¹⁶

The SE rate is given by

$$\sigma = \eta + \delta = \frac{I_{\text{BE}} + I_{\text{SE}}}{I_0} = \frac{I_0 + I(x < 0)}{I_0} = 1 + \frac{I(x < 0)}{I_0}, \quad (19)$$

where $I(x < 0)$ is the “resulting” electron current into the vacuum diminished, of course, by the impinging reverse moving PE beam current I_0 . So we have to add, again, I_0 to $I(x < 0)$ in order to get the real emission current ($I_{\text{BE}} + I_{\text{SE}}$) and the respective fractions ($\eta + \delta$).

We may observe the time dependence of the surface potential $V_0(t)$ and the secondary emission $\sigma(t)$ presented in Figs. 6 and 7, respectively.

As we have already mentioned, the positive charging at $E_0 = 1 \text{ keV}$ is limited by the grounded surrounding (grid potential $V_G = 0$). So, V_0 passes a maximum of $V_0 = +4.6 \text{ V}$ after $t \approx 5 \text{ ms}$, and is then decaying to about $V_0 = +4.35 \text{ V}$

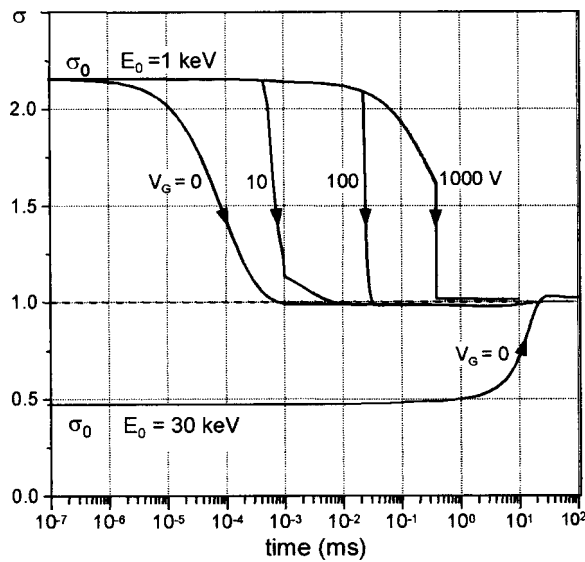


FIG. 7. Rapid change of the secondary electron emission fraction $\sigma = \eta + \delta$ with irradiation time t for $E_0 = 1$ and 30 keV, respectively, and different vacuum grid potentials V_G . The initial value $\sigma_0(t \rightarrow 0)$ corresponds to the noncharged Al_2O_3 sample; the final steady state for the bulk sample ($d = 3$ mm) should always approach $\sigma = 1$ ($j_0 = 10^{-5}$ A/cm 2).

for times $t > 30$ ms. On the other hand, the negative charging at $E_0 = 30$ keV is not limited by returning SEs (or TEs), even SEs are enforced to leave the negative surface, and the surface potential approaches a saturation with $V_0 \approx -21$ kV after $t \geq 20$ ms. Of course, this huge negative charging has led to a retarding of the primary electron beam. This retarding of incident PEs is correlated with a decrease of the maximum electron range $R(E'_0)$ within the insulating sample.

In Fig. 7 the time-dependent SE rates $\sigma(t)$ are presented. Clearly, we recognize the blocked SEE to $\sigma = 1$ for $E_0 = 1$ keV after $1 \mu\text{s}$ as well as the increase of SEE for $E_0 = 30$ keV. The latter one is caused by PE retarding due to the negative surface potential $V_0 < 0$ and, consequently, by a higher SE rate $\sigma(E'_0)$. Because the backscattering electron fraction of Al_2O_3 with $\eta \approx 0.18$ is nearly constant the true SE rate $\delta_0(E_0 = 30 \text{ keV}, t = 0) = 0.35$ has increased to $\delta(E'_0 \approx 8 \text{ keV}, t > 20 \text{ ms}) \approx 0.82$. Indeed, this is a drastic change of the SE emission rate due to the negative charging within the insulators. The steady state $\sigma = 1$ is obtained after about 25 ms.

Let us now investigate the influence of the grid potential V_G (hitherto, we have considered only $V_G = 0$). In Fig. 7 we see a drastic change of the σ slope with time when increasing the grid potential V_G to +10, +100, and +1000 V. Now, obviously, the surface will be charged more positively and it takes more time until the surface potential V_0 reaches the positive grid potential V_G and starts the retarding process according to Eq. (16).

Indeed, when looking to the time-dependent and final steady state charge distributions in Figs. 8(a) and 8(b), respectively, we see that the grid potential considerably controls the incorporated charge. For high grid voltages $V_G = +1000$ V, even we get a plus-minus-plus-minus charge distribution instead of a minus-plus-minus one obtained for lower V_G . Also, the range of incorporated charges increases

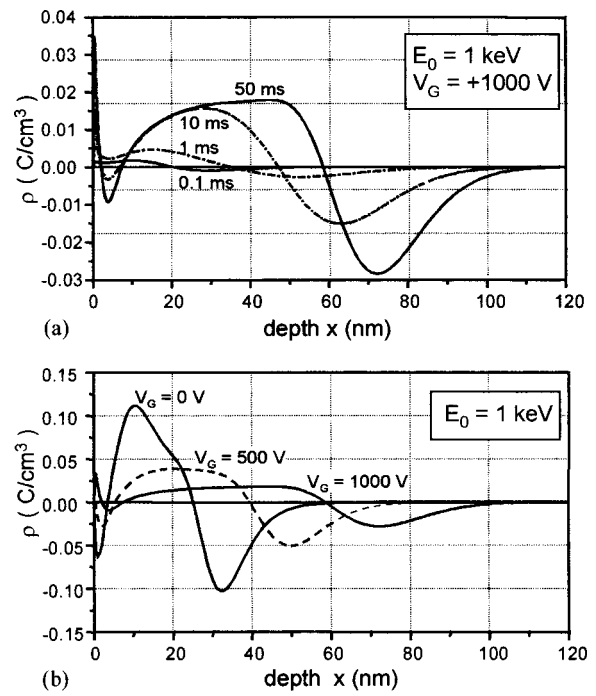


FIG. 8. Charge distributions $\rho(x)$ for a low energy injection $E_0 = 1$ keV and different vacuum grid potentials V_G , (a) in dependence on irradiation time for $V_G = +1000$ V; (b) final steady state distributions for different V_G .

with V_G . That indicates that the surface potential V_0 has become more positive and the incident beam energy is increased by $+eV_0$.

Generally, we may state that the actual retarded or elevated electron beam energy E'_0 is diminished or increases by the surface potential V_0 :

$$E'_0 = E_0 + eV_0. \tag{20}$$

Thus, in Fig. 9 we have plotted the maximum range R versus

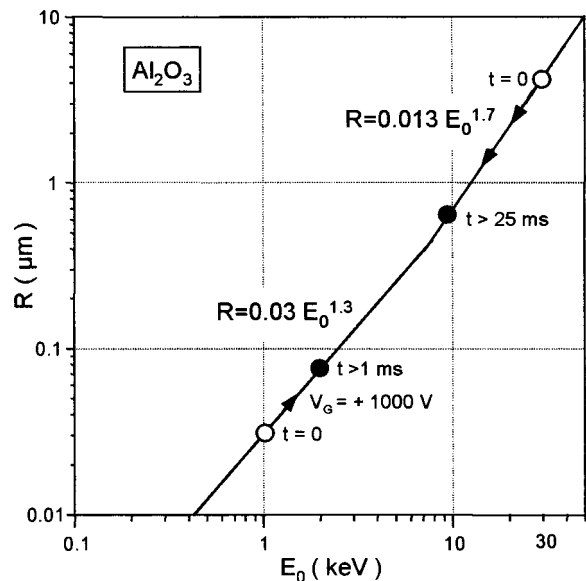


FIG. 9. Maximum range $R(E_0)$ of primary electrons in noncharged Al_2O_3 targets (\circ) retarded by negative charging at $E_0 = 30$ keV to a much lower value $E'_0 \approx 9$ keV (\bullet) as well as accelerated at $E_0 = 1$ keV and $V_G = +1000$ V to $E'_0 \approx 2000$ keV (\bullet).

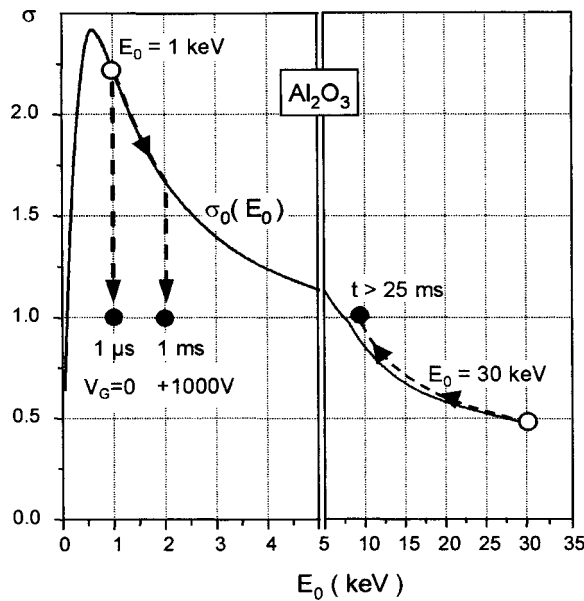


FIG. 10. Initial rate (○) of secondary electrons $\sigma_0(E_0)$ from Al_2O_3 as a function of the PE energy E_0 as well as its change by charging to $\sigma(E'_0)$ (●) [in context with Eq. (20)]; sample thickness $d = 3$ mm.

the initial beam energy E_0 as given in Eqs. (2a) and (2b) and have compared it with the resulting actual range $R(E'_0)$ obtained in the final steady state of irradiation, i.e., in the case of $E_0 = 30$ keV after $t > 25$ ms. Obviously, the observed value $R(E'_0) \approx 0.9 \mu\text{m}$ corresponds to an actual retarded or enhanced beam energy $E'_0 \approx 9$ keV according to Eq. (20). Of course, this value is expected from the surface potential $V_0 = -21$ kV in context with Eqs. (20) and (2b). Then, let us check the other accessible quantity, the SE rate σ . In Fig. 10 we have plotted the initial SE rate $\sigma_0(E_0) = \sigma(E_0, t = 0)$, i.e., the real material-dependent SE rate from fresh and non-charged samples. With our calculations we obtain a maximum of the SE rate $\sigma_0(E_0 = 0.7 \text{ keV}) = 2.4$. This corresponds approximately to the experimental values presented by Seiler¹⁰ with $\sigma_{\text{max}} = 2.6 - 4.7$, but it is considerably smaller than the maximum value $\sigma_{\text{max}} \approx 6.4$ of Dawson.⁴⁰ The first sigma-unit point is found with $\sigma_0(E'_0 = 50 \text{ eV}) = 1$ and the second one at $\sigma_0(E''_0 = 8.4 \text{ keV}) = 1$.

Further on, in the case of thick insulating samples, the SE rate will approach very rapidly the steady state with $\sigma = 1$. We see in Figs. 9 and 10 that the negative charging for high beam energies $E_0 = 30$ keV never will approach so high values that the retarded electron range $R(E'_0)$ would be comparable with the SE maximum escape depth of about 25 nm as predicted by the Cazaux model.⁷ This point is related to the fact that the slowing-down of the electrons is mostly due to the negative surface voltage and less to an inner slowing down as described by Cazaux. Moreover, the retarded energy $E'_0 = 9$ keV approaches almost the second sigma-unit point $E''_0 = 8.4$ keV and the conventional bipolar model is nearly fulfilled.

On the other hand, for low beam energies $E_0 = 1$ keV and positive charging $V_0 > 0$, the initial SE rate $\sigma_0 > 1$ will be suppressed very rapidly down to $\sigma = 1$ by a grounded vacuum electrode or grid biased to $V_G = 0$. So, the surface

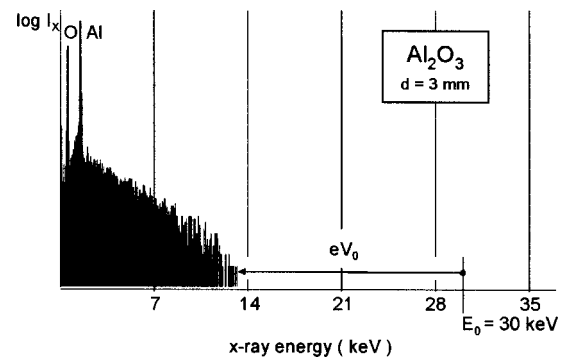


FIG. 11. Measurement of the negative surface potential V_0 by means of the energy-dispersive x-ray bremsstrahlung (BS) threshold shift: $E'_x = E_0 + eV_0 = E''_0$, initial beam energy $E_0 = 30$ keV.

potential approaches only small positive values of $V_0 \approx + (4 - 5)$ eV, as we have seen also in Fig. 6(a). But, increasing the voltage potential to $V_G = +1000$ V, $\sigma(E_0)$ follows the surface potential up to $V_0 = +1002$ V, i.e., to $E'_0 = 2002$ eV, and then drops rapidly to the final steady state $\sigma = 1$. Also, here, the bipolar model in its tendency is fulfilled but the positive charging is limited, again, by the controlling grid voltage V_G .

In order to prove the accessible quantities $V_0(t)$ and $\sigma(t)$, we have chosen two experiments. The first one is measuring the surface potential V_0 by means of the x-ray bremsstrahlung (BS) spectra, i.e., by the shift of the short wavelength threshold due to the negative surface potential V_0 and respective retarding of the PE beam according to Eq. (20). This method has been proposed already by other authors, e.g., by Belhaj *et al.*⁶ In Fig. 11 this effect is demonstrated for the 3 mm Al_2O_3 sample and $E_0 = 30$ keV electron beam irradiation. We observe the BS shortwave limit at $E_x = 13$ keV; that corresponds to a negative surface potential of $V_0^{\text{exp}} = -17$ kV. Comparing this with our simulation value of $V_0 = -21$ kV from Figs. 6 and 10, we recognize a worse isolation behavior of the real experimental Al_2O_3 target than of the simulated one. Indeed, this was expected and, nevertheless, it demonstrates the right tendency of huge negative charging of thick insulating samples under high energy electron beam irradiation with $\sigma_0(E_0) < 1$. Concerning the second accessible quantity $\sigma(t)$, it can be deduced from the measurement of the overall target support current I_M .²¹ These results will be detailed elsewhere.

VI. CONCLUSIONS

The one-dimensional approach of ballistic electron and hole transport allows us to simulate the self-consistent charging-up process in bulk insulators. Because of the great thickness of the insulating samples, the surface potential V_0 changes very rapidly and controls the further incorporation of charges. At high electron beam energies $E_0 = 30$ keV the surface potential becomes strongly negative and the electron beam is decelerated down to $E'_0 = E_0 + eV_0 \approx 9$ keV near to the second sigma-unit value $\sigma(E''_0 = 8.4 \text{ keV}) = 1$. Thus, the bipolar model of opposite charging is nearly fulfilled. On the other hand, the charge beneath the surface is positive because

of the favored SE escape and we obtain a plus–minus–plus–minus spatial charge structure with prevailing minus parts within the bulk insulator.

For low energy electron bombardment $E_0 \approx 1$ keV the rapid positive charging suppresses a field-enhanced SE escape and the steady state with $j(x,t) = \text{const} = 0$, and $\sigma = 1$ produces a minus–plus–minus charge distribution. Now, the surface potential is only weakly positive and exceeds that of the grounded SEM chamber ($V_G = 0$) only by $V_0 = +4.5$ V. But, for higher grid potentials V_G up to $+1000$ V and $E_0 = 1$ keV, the positive charging is much greater and approaches $V_0 \approx V_G$. Thus, the beam energy amounts $E'_0 = E_0 + eV_G$ and tries to approach the second sigma-unit point E_0^{II} . Here, the bipolar model also becomes valid.

The experimental methods of the bremsstrahlung shift allows us to measure the surface potential V_0 . The experimental result is still in sufficient agreement with our self-consistent simulation of the charging process.

ACKNOWLEDGMENTS

The authors wish to acknowledge D. Juvé for valuable measurements and G. Damamme for fruitful discussions.

- ¹Proceedings of the 4th International Conference on Electric Charges in Non-Conductive Materials, Le Vide: Science, Techniques et Applications (2001), Vol. Special CSC'4.
- ²G. Blaise and W. J. Sarjeant, IEEE Trans. Dielectr. Electr. Insul. **5**, 779 (1998).
- ³L. Levy, Space Technology Course, Cepadues Editions, Toulouse, France (2002), p. 241.
- ⁴V. Griseri, L. Levy, D. Payan, T. Maeno, K. Fukunaga, and C. Laurent, *Annual Report: Conference on Electrical Insulation and Dielectric Phenomena* (Omni, Piscataway, NJ, 2002), p. 922.
- ⁵J. Cazaux, J. Electron Spectrosc. Relat. Phenom. **105**, 155 (1999).
- ⁶M. Belhaj, O. Ibara, M. N. Filippov, E. I. Rau, and M. V. Andrianov, Appl. Surf. Sci. **177**, 58 (2001).
- ⁷J. Cazaux, J. Appl. Phys. **89**, 8265 (2001).
- ⁸H. Kimura and I. Mann, Earth, Planets Space **51**, 1223 (1999).
- ⁹O. Hachenberg and W. Brauer, Adv. Electron. Electron Phys. **11**, 413 (1959).
- ¹⁰H. Seiler, Z. Angew. Phys. **22**, 249 (1967).
- ¹¹P. H. Dawson, J. Appl. Phys. **37**, 3644 (1966).

- ¹²L. Reimer, *Scanning Electron Microscopy*, Springer Series in Optical Sciences (Springer, Berlin, 1985), Vol. 45.
- ¹³O. Hachenberg and W. Brauer, Scanning Microsc. **4**, 57 (1990).
- ¹⁴A. Melchinger and S. Hofmann, J. Appl. Phys. **78**, 6224 (1995).
- ¹⁵J. Cazaux, J. Appl. Phys. **85**, 1137 (1999).
- ¹⁶H.-J. Fitting, H. Glaefcke, W. Wild, M. Franke, and W. Müller, Exp. Tech. Phys. (Berlin) **27**, 13 (1979).
- ¹⁷I. A. Glavatskikh, V. S. Kortov, and H.-J. Fitting, J. Appl. Phys. **89**, 440 (2001).
- ¹⁸E. Vicario, N. Rosenberg, and R. Renoud, Surf. Interface Anal. **22**, 115 (1994).
- ¹⁹J. P. Ganachaud, C. Attard, and R. Renoud, Phys. Status Solidi B **199**, 175 (1997); **199**, 455 (1997).
- ²⁰R. Renoud, F. Mady, and J. P. Ganachaud, J. Phys.: Condens. Matter **14**, 231 (2002).
- ²¹X. Meyza, Ph.D. thesis, Ecole Supérieure des Mines de Saint-Etienne (2003).
- ²²L. Malter, Phys. Rev. **49**, 478 (1936).
- ²³H.-J. Fitting, H. Glaefcke, and W. Wild, Phys. Status Solidi A **43**, 185 (1977).
- ²⁴C. A. Klein, J. Appl. Phys. **39**, 2029 (1968).
- ²⁵R. C. Alig and S. Bloom, Phys. Rev. Lett. **35**, 1522 (1975).
- ²⁶H.-J. Fitting, H. Glaefcke, W. Wild, and R. Ulbricht, Exp. Tech. Phys. (Berlin) **24**, 447 (1976).
- ²⁷Th. Hingst, M. Hübner, R. Franz, Ch. Kuhr, and H.-J. Fitting, Microelectron. Eng. **24**, 181 (1994).
- ²⁸H.-J. Fitting and J.-U. Friemann, Phys. Status Solidi A **69**, 349 (1982).
- ²⁹H.-J. Fitting and J. Boyde, Phys. Status Solidi A **75**, 137 (1983).
- ³⁰E. Schreiber and H.-J. Fitting, J. Electron Spectrosc. Relat. Phenom. **124**, 25 (2002).
- ³¹H.-J. Fitting, H. Glaefcke, and W. Wild, Surf. Sci. **75**, 267 (1978).
- ³²D. Dew-Hughes and O. H. Wyatt, *Metals, Ceramics and Polymers* (Cambridge University Press, New York, 1974).
- ³³D. R. Lide, *Handbook of Chemistry and Physics*, 83rd ed. (CRC Gaithersburg, MD, 2001).
- ³⁴W. H. Strehlow and E. L. Cook, J. Phys. Chem. **2**, 163 (1973).
- ³⁵A. H. Sommer, *Photoemission Materials* (Wiley, New York, 1968).
- ³⁶T. H. Ning, J. Appl. Phys. **47**, 3203 (1976).
- ³⁷I. I. Milman, V. S. Kortov, and S. V. Nikiforov, Radiat. Meas. **29**, 401 (1998).
- ³⁸V. A. J. Van Lint, J. M. Bunch, and T. M. Flanagan, in Proceedings of the Conference on Radiation Effects and Tritium Technology for Fusion Reactors, edited by J. S. Watson, F. W. Wiffen, I. L. Bishop, and B. K. Breeden, Gatlinburg, TN (1976), Vol. 11, p. 531.
- ³⁹P. C. Srivasta, A. Roy Bardhan, and D. L. Bhattacharya, Int. J. Electron. **46**, 547 (1979).
- ⁴⁰P. H. Dawson, J. Appl. Phys. **37**, 3644 (1966).